PHYSICAL REVIEW C **105**, 034343 (2022)

Low-energy monopole strength in spherical and axially deformed nuclei: Cluster and soft modes

F. Mercier,[1] J.-P. Ebran,[2,3] and E. Khan[1]
[1]*IJCLab, Université Paris-Saclay, IN2P3-CNRS, F-91406 Orsay Cedex, France*
[2]*CEA, DAM, DIF, F-91297 Arpajon, France*
[3]*Université Paris-Saclay, CEA, Laboratoire Matière en Conditions Extrêmes, F-91680 Bruyères-le-Châtel, France*

(Received 7 September 2021; revised 4 February 2022; accepted 17 March 2022; published 30 March 2022)

Background: Several recent experiments report significant low-energy isoscalar monopole strength, below the giant resonance, in various nuclei. In light α-conjugate nuclei, these low-energy resonances were recently interpreted as cluster vibration modes. However, the nature of these excitations in neutron-rich nuclei remains elusive.
Purpose: The present work provides a systematic analysis of the low-energy monopole strength in isotopic chains, from neon to germanium, in order to monitor and understand its nature and conditions of emergence.
Methods: We perform covariant quasiparticle random phase approximation calculations, formulated within the finite amplitude method, on top of constrained relativistic Hartree-Bogoliubov (RHB) reference states.
Results: Neutron excess leads to the appearance of low-energy excitations according to a systematic pattern reflecting the single-particle features of the underlying RHB reference state. With the onset of deformation, these low-energy resonances get split and give rise to more complex patterns, with possible mixing with the giant resonance. At lower energy, clusterlike excitations found in $N = Z$ systems survive in neutron-rich nuclei, with valence neutrons arranging in molecularlike orbitals. Finally, at very low energy, pair excitations are also found in superfluid nuclei, but remain negligible in most of the cases.
Conclusions: The low-energy part of the monopole strength exhibits various modes, from cluster vibrations ($\approx$5–10 MeV) to components of the giant resonance downshifted by the onset of deformation, including soft modes ($\approx$10–15 MeV) as well as pair excitation ($<$5 MeV), with possible mixing, depending on neutron excess, deformation, and pairing energy.

DOI: 10.1103/PhysRevC.105.034343

I. INTRODUCTION

The complex nature of nuclear many-body systems is reflected in the vast diversity of their structure properties and excitation modes. In stable nuclei, the response to an external perturbation is dominated by collective modes, involving the coherent superposition of particle-hole excitations, coined giant resonances (GRs). The structural evolution of nuclei as one drifts away from the valley of β-stability—e.g., the onset of static correlations responsible for nuclear deformation, superfluidity, and clustering; the exotic arrangements of nucleons stemming from an increasing unbalance between the neutron and proton number; the impact of the loosely bound nature of nucleon orbitals and proximity of the continuum, etc.—yields an enrichment of the ways a nucleus responds to an external probe. Namely, in such cases, one observes a redistribution of the strength functions towards lower energy, below the GRs, associated with the emergence of new, exotic patterns of excitation [1–3]. The nature of these new excitations has been studied in different multipolarities and appears to be twofold, namely, (i) so-called soft modes involving neutron excitations [4–9], sometimes associated with resonant oscillations of a neutron skin against a tightly bound core, and (ii) cluster vibrations [10–14].

Soft modes have attracted much attention both from the experimental [2,3,15–20] and theoretical perspectives, with various approaches used to pin down their properties, including the (quasiparticle) random phase approximation [(Q)RPA] [21–23], the (quasiparticle) finite amplitude method [(Q)FAM] [5,24], and the multiphonon quasiparticle-phonon model [25–28]. Most of the studies on soft modes have focused on dipole resonances and/or spherical systems (see, however, Ref. [29] for a discussion of monopole soft modes in neutron-rich deformed nuclei). A comprehensive understanding of the evolution of the low-energy part of the isoscalar monopole (ISM) strength, with isospin asymmetry and deformation, is still lacking.

On the other hand, cluster modes have mostly been investigated in light $N = Z$ nuclei, both within the antisymmetrized molecular dynamics (AMD) and energy density functional (EDF) approaches [10–14]. How neutron excess interferes with such cluster modes remains an open question. From a more general point of view, the interplay between soft, cluster and GR modes, and their evolution with isospin asymmetry and deformation, have not been established in a single approach, mainly because of the lack of a microscopic theoretical framework capable of simultaneously tackling these various modes within a computationally affordable effort.

Recently, relativistic EDFs were shown to consistently describe both liquidlike and clusterlike features of nuclei, be it their ground-state [30–33] or spectroscopic (energies of excited states, reduced probability transition, elastic and inelastic form factors, etc.) properties [34,35]. Since a covariant formulation of the quasiparticle random phase approximation (QRPA) is known to correctly describe GRs and soft modes [21,23,36,37], on one hand, as well as cluster vibrations [14], on the other hand, it shall be a tool of choice for achieving a global understanding of the mechanisms driving the emergence of these modes. In this study, the covariant QRPA is implemented under the form of the QFAM [37,38], which significantly lowers the computational cost compared to the traditional matrix formulation. This approach allows one to provide an in-depth study of the impact of (i) isospin asymmetry, (ii) deformation, and (iii) pairing correlations, as well as their interplay on the structure of the ISM strength.

The paper is organized as follows. In Sec. II, we briefly introduce the covariant QFAM formalism. The evolution of the ISM strength with isospin asymmetry is extensively discussed in the simple case of spherical nuclei, in Sec. III. Section IV is dedicated to the consequences of the onset of deformation on the properties of the ISM strength. Finally, in Sec. V, we analyze the role played by pairing correlations in driving the emergence of another type of low-energy resonance.

II. QFAM THEORETICAL FRAMEWORK

The FAM was first proposed by Ref. [39] for a nonsuperfluid spherical system and quickly extended to superfluid ones [40]. The consideration of the deformation effect was then added [41] and the framework was extended to covariant (Q)FAM [36,37]. The present implementation of the covariant QFAM is based on Ref. [38].

In the QFAM formalism, an external time-dependent field,

$$F(t) = \eta[F(\omega)e^{-i\omega t} + F^\dagger(\omega)e^{+i\omega t}], \tag{1}$$

with η a real, small parameter, induces a linear response of the system, characterized by the following equations, in the quasiparticle (qp) basis:

$$(E_\mu + E_\nu - \omega)X_{\mu\nu}(\omega) + \delta H^{20}_{\mu\nu}(\omega) = -F^{20}_{\mu\nu}, \tag{2a}$$

$$(E_\mu + E_\nu + \omega)Y_{\mu\nu}(\omega) + \delta H^{02}_{\mu\nu}(\omega) = -F^{02}_{\mu\nu}. \tag{2b}$$

They describe the oscillation of the system around a static configuration, which is the solution of a constrained relativistic Hartree-Bogoliubov (RHB) equation,

$$\begin{pmatrix} h(\boldsymbol{q}) - \lambda & \Delta(\boldsymbol{q}) \\ -\Delta^*(\boldsymbol{q}) & -h^*(\boldsymbol{q}) + \lambda \end{pmatrix}\begin{pmatrix} U_\mu(\boldsymbol{q}) \\ V_\mu(\boldsymbol{q}) \end{pmatrix} = E_\mu(\boldsymbol{q})\begin{pmatrix} U_\mu(\boldsymbol{q}) \\ V_\mu(\boldsymbol{q}) \end{pmatrix}. \tag{3}$$

E_μ, U_μ, and V_μ stand for the energy and wave function of the qp μ. The fields $h[\rho]$ and $\Delta[\kappa]$, functionals of the one-body normal and anomalous density matrices $\rho = V^*V^T$ and $\kappa = V^*U^T$, are the RHB mean potential in the particle-hole and particle-particle channels, respectively. λ is the chemical potential and $\boldsymbol{q}$ collects a set of constrained collective coordinates (e.g., deformation parameters, pairing gap, etc.). $X_{\mu\nu}(\omega)$ and $Y_{\mu\nu}(\omega)$ are the QFAM amplitudes at a given excitation energy ω, and $\delta H^{20(02)}$ ($F^{02(02)}$) represent the 2qp components of the induced Hamiltonian (external perturbation). Namely, if $F(\omega)$ is a one-body operator, represented by the matrix elements f,

$$F(\omega) = \sum_{ij} f_{ij} c_i^\dagger c_j = \frac{1}{2}(c^\dagger \quad c)\begin{pmatrix} f & 0 \\ 0 & -f^T \end{pmatrix}\begin{pmatrix} c \\ c^\dagger \end{pmatrix} \tag{4}$$

(where a constant term was neglected), then

$$\begin{aligned} &\begin{pmatrix} F^{11} & F^{20} \\ F^{02} & -(F^{11})^T \end{pmatrix} \\ &\equiv \mathcal{W}^\dagger \begin{pmatrix} f & 0 \\ 0 & -f^T \end{pmatrix}\mathcal{W} \\ &= \begin{pmatrix} U^\dagger f U - V^\dagger f^T V & U^\dagger f V^* - V^\dagger f^T U^* \\ V^T f U - U^T f^T V & V^T f V^* - U^T f^T U^* \end{pmatrix}, \end{aligned} \tag{5}$$

where $\mathcal{W}$ is the unitary Bogoliubov transformation, by which the qp ladder operators $\beta^\dagger$ and β are expressed as linear combinations of the single-particle (sp) operators c and $c^\dagger$,

$$\begin{pmatrix} \beta \\ \beta^\dagger \end{pmatrix}\begin{pmatrix} U^\dagger & V^\dagger \\ V^T & U^T \end{pmatrix}\begin{pmatrix} c \\ c^\dagger \end{pmatrix} \equiv \mathcal{W}^\dagger \begin{pmatrix} c \\ c^\dagger \end{pmatrix}. \tag{6}$$

Likewise, by denoting, in the sp basis, the induced fields in the particle-hole and particle-particle channels by $\delta h(\omega)$ and $\delta\Delta^{(\pm)}(\omega)$, respectively, we have

$$\begin{pmatrix} \delta H^{11} & \delta H^{20} \\ -\delta H^{02} & -(\delta H^{11})^T \end{pmatrix} \equiv \mathcal{W}^\dagger \begin{pmatrix} \delta h & \delta\Delta^{(+)} \\ -\delta\Delta^{(-)*} & -\delta h^T \end{pmatrix}\mathcal{W}, \tag{7}$$

i.e.,

$$\begin{aligned} \delta H^{20}(\omega) = {} & U^\dagger \delta h(\omega) V^* + U^\dagger \delta\Delta^{(+)}(\omega) U^* \\ & - V^\dagger \delta\Delta^{(-)*}(\omega) V^* - V^\dagger \delta h^T(\omega) U^* \end{aligned} \tag{8}$$

and

$$\begin{aligned} \delta H^{02}(\omega) = {} & - V^T \delta h(\omega) U - V^T \delta\Delta^{(+)}(\omega) V \\ & + U^T \delta\Delta^{(-)*}(\omega) U + U^T \delta h^T(\omega) V. \end{aligned} \tag{9}$$

The perturbed fields δh and $\delta\Delta^{(\pm)}$ can be expressed in terms of the static RHB fields h and Δ (after linearizing the explicit density-dependent parts of the covariant energy density functional) and the induced normal and anomalous density matrices, that is,

$$\delta h(\omega) = h[\delta\rho(\omega)], \tag{10a}$$

$$\delta\Delta^{(+)}(\omega) = \Delta[\delta\kappa^{(+)}(\omega)], \tag{10b}$$

$$\delta\Delta^{(-)}(\omega) = \Delta[\delta\kappa^{(-)}(\omega)], \tag{10c}$$

and

$$\delta\rho(\omega) = UX(\omega)V^T + V^*Y^T(\omega)U^\dagger, \tag{11a}$$

$$\delta\kappa^{(+)}(\omega) = UX(\omega)U^T + V^*Y^T(\omega)V^\dagger, \tag{11b}$$

$$\delta\kappa^{(-)}(\omega) = UY^*(\omega)U^T + V^*X^\dagger(\omega)V^\dagger. \tag{11c}$$

The latter depend on the QFAM amplitudes X and Y, making the master equations (8) and (9) self-consistent.

In the QFAM formalism, the strength function derives from

$$S(f, \omega) = -\frac{1}{\pi}\mathrm{Im}\mathrm{Tr}[f^\dagger \delta\rho(\omega)]. \tag{12}$$

The electric isoscalar multipole operator reads

$$f_{JK}^{IS} = \sum_{i=1}^{A} f_{JK}(\mathbf{r}_i), \tag{13}$$

with $f_{JK}(\mathbf{r}) = r^J Y_{JK}(\theta, \phi)$. In the case of the monopole mode, $f_{00}(\mathbf{r}) = r^2$. For an even-even axially symmetric nucleus, the operators f_{JK} and f_{J-K} yield identical strength functions. QFAM calculations can therefore be simplified by using the operator $f_{JK}^{(+)} = [f_{JK} + (-1)^K f_{J-K}]/\sqrt{2+2\delta_{K0}}$, and assuming $K \geqslant 0$.

In this study, the QFAM calculations are based on the DD-PC1 energy density functional [42], complemented by a separable pairing force in momentum space [43,44]: $\langle k|V^{^1S_0}|k'\rangle = -Gp(k)p(k')$ in the particle-particle channel. By assuming a simple Gaussian ansatz $p(k) = e^{-a^2k^2}$, the two parameters G and a were adjusted to reproduce the density dependence of the pairing gap at the Fermi surface, obtained in nuclear matter with the Gogny D1S parametrization [45]. In practice, we first compute the U and V RHB matrices and qp energies E_μ, after solving the RHB equations for a nucleus of interest, expanded in an axially symmetric harmonic oscillator basis. The QFAM procedure then consists of starting with a trial set of X's and Y's, computing the induced density matrices (11a)–(11c), then the perturbed mean fields (10a)–(10c), and, finally, H^{20} and H^{02}, according to Eqs. (8) and (9). Solving (2a) and (2b) then yields a new set of X's and Y's, from which the previous steps are repeated until convergence. Further details on the QFAM solver DIRQFAM can be found in Ref. [38].

The obtained QFAM amplitudes [Eqs. (2a) and (2b)] and the strength function (12) are defined in the whole complex ω-plane, except at the QRPA eigenenergies where they diverge. In practice, calculations are performed for excitation energies $\omega + i\gamma$, with a fixed imaginary part γ: this corresponds to a Lorentzian smearing of the strength function, with the width $\Gamma = 2\gamma$ [40]. The smearing is fixed to $\Gamma = 0.5$ MeV for all the calculations. The size of the basis, in which the RHB-QFAM equations are expanded, runs from 13 to 15 shells, depending on the mass of the nucleus. It ensures the convergence of our results below 1%. As explained in [14], the part of the strength with $\omega > 20$ MeV may not be stable with respect to the size of the basis. However, the position of the Giant Monopole Resonance (GMR) centroids remains stable and we aim to focus on the low-energy part of the strength.

We have checked that the single qp spectrum and, hence, the QFAM results are not strongly impacted by the choice of the constraint operator. For this purpose, Fig. 1 shows the difference in the single qp spectrum and on the QFAM response, using two different ways to constrain the calculation: either with a quadrupolar moment on both neutron and proton or a constraint rms radius. The difference is negligible and does not impact the QFAM response very much.

III. EVOLUTION OF LOW-ENERGY ISOSCALAR MONOPOLE MODES WITH ISOSPIN ASYMMETRY

We start by investigating the impact of the isospin asymmetry on the properties of low-energy ISM modes by first focusing on the single open-shell $Z = 20$ and $Z = 28$ nuclei: the vanishing of deformation, at the mean-field level, simplifies the pattern of excitation. Moreover, the abundance of both experimental and theoretical results shall enable one to benchmark the present calculations.

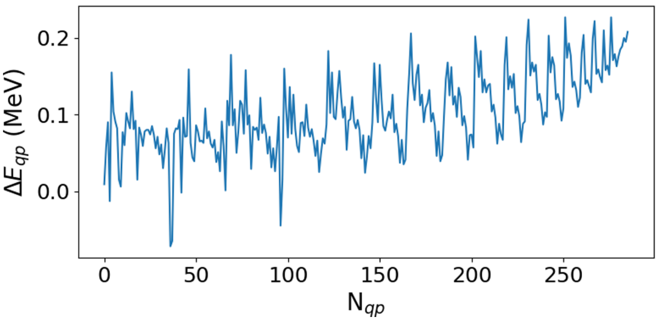

FIG. 1. Differences in the qp proton energies obtained with quadrupolar constraint on neutron and proton vs constraint on the rms radius.

A generic pattern of emergence of low-energy ISM modes, as the neutron over proton numbers ratio rises, can be traced back to the mismatch between the neutron and proton Fermi energies due to increasingly bound protons and, conversely, last occupied neutron orbitals getting closer to the continuum. As a result, valence neutrons decouple from the other nucleons and participate to excited modes of a rather noncollective nature. These modes appearing with neutron (or proton) excess will be hereafter referred to as soft modes. In other words, the emergence of new low-energy ISM modes, with increasing neutron number, can be understood from the single-particle (sp) structure, i.e., the sp spectrum of the reference RHB state, on top of which the QRPA response is built: the appearance of a peak, in the low-energy strength, coincides with the filling of an orbital with spherical quantum numbers n, j, l, m, from which an additional 2qp configuration $[njlm; (n+1)jlm]^{J=0}$ becomes available. The ISM strength therefore reflects the energy pattern of the sp spectrum: (i) appearance of low-energy resonances, on top of the main part of the strength, whenever an orbital inaugurating a new major shell starts to get filled, and (ii) increase of the strength in a small energy window, as long as orbitals of the same major shell are getting filled. The decrease of the corresponding excitation energy, as one goes from a major shell to the next one, mainly stems from the weakening of the binding energies of valence neutrons, i.e., the shrinking of the gap between the occupied n and empty $n+1$ orbitals involved in the ISM transition. This specific pattern shall be illustrated on the $Z = 20$ and $Z = 28$ isotopic chains, in the next two sections.

A. Calcium isotopes

The distribution of ISM strength computed with the covariant QFAM in the even-even $^{40-62}$Ca isotopes is displayed in Fig. 2. While the GMR ($\omega \approx 18$ MeV) remains quite stable along the isotopic chain, the structure of the low-energy part of the ISM strength changes with neutron excess. This can be understood with the Ca canonical single-neutron spectra,

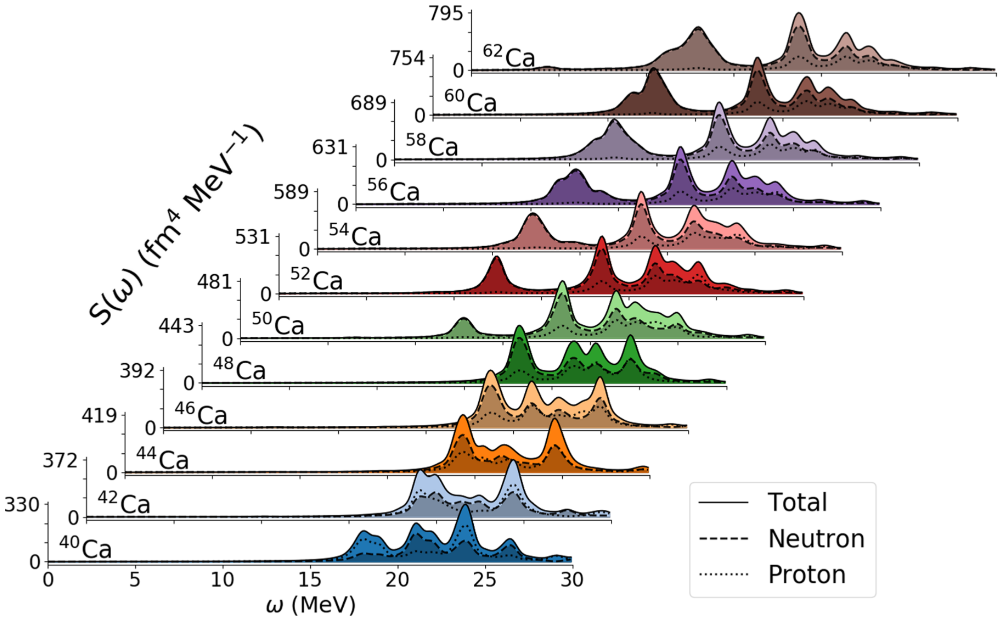

FIG. 2. Distribution of the isoscalar monopole strength in the Ca isotopic chain obtained within the covariant QFAM with the DD-PC1 parametrization, split into total (solid line), neutron (dashed line), and proton (dotted line) contributions.

plotted against mass number, in Fig. 3: in ^{42}Ca, two neutrons fill the $1f_{7/2}$ orbital, opening the $1f_{7/2} \rightarrow 2f_{7/2}$ transition as a possible contribution to the ISM response. A decomposition of ^{42}Ca monopole resonances into 2-qp components shows that the $1f_{7/2} \rightarrow 2f_{7/2}$ transition mainly contributes to a peak located at $\omega \approx 20$ MeV, which is in the GMR. As discussed above, going to the next major shell, i.e., adding two neutrons in the $2p_{3/2}$ orbital after filling the $1f_{7/2}$ orbital—that is, ^{50}Ca—is expected to generate a low-energy resonance separated from the main part of the ISM strength. As also discussed above, filling the orbitals inside the same major shell, i.e., from the $2p_{3/2}$ to the $1g_{9/2}$ levels, is expected to generate contributions to the strength in the same energy window. Indeed, the filling of each of the orbitals, from $2p_{3/2}$ to $1g_{9/2}$, gives rise to excitations close in energy (see Fig. 3), each of them dominated by a single 2qp configuration. Namely, in ^{50}Ca, one finds a 12.8 MeV excitation mode (see Fig. 2 and Table I) for which the dominant 2qp contribution (carrying 40% of the total 2qp contributions) is $2p_{3/2} \rightarrow 3p_{3/2}$, in agreement with the results of Refs. [6,7,46]. In ^{54}Ca, a small peak appears at 14.7 MeV, corresponding to the $2p_{1/2} \rightarrow 3p_{1/2}$ transition. In ^{56}Ca, a resonance at 11.5 MeV emerges from the filling of the $1f_{5/2}$ orbital and the $1f_{5/2} \rightarrow 2f_{5/2}$ transition. In ^{62}Ca, the filling of the $1g_{9/2}$ and, hence, the $1g_{9/2} \rightarrow 2g_{9/2}$ transition triggers a resonance at 12 MeV. This last excitation is, however, not dominant and is not clearly visible in the strength. However, the details of the qp contributions indicate that this transition holds for about 10% of the strength between 10 and 13 MeV. It should be noted that another resonance is visible around 4 MeV in ^{62}Ca, whose nature will be discussed in Sec. V.

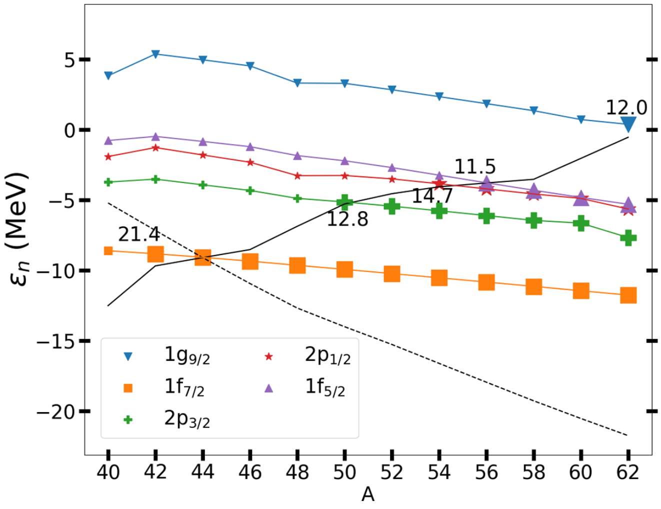

FIG. 3. RHB single-particle spectrum in Ca isotopes. The neutron (proton) Fermi energy is represented by a black solid (dashed) line. Empty (occupied) orbitals are designated by small (large) markers. Numbers indicate the energy of the resonance associated to the filled orbital.

The properties of the low-energy neutron modes can be further studied by computing their corresponding transition densities defined as

$$\delta\rho^{\mathrm{tr}}(\boldsymbol{r}) = -\frac{1}{\pi}\mathrm{Im}[\delta\rho(\boldsymbol{r})], \tag{14}$$

where $\delta\rho(\boldsymbol{r})$ is computed using Eq. (11a). These transition densities are plotted in Fig. 4. For the sake of comparison, the upper left panel displays the transition densities of the GMR in ^{40}Ca, with its typical in-phase oscillation of protons and neutrons. The properties of the different modes are detailed in Table I. The transition densities associated to the low-lying modes at $\omega = 12.8$ MeV in ^{50}Ca and at $\omega = 12.6$ MeV in ^{60}Ca show a very different behavior compared to the GMR in ^{40}Ca. As described in Ref. [7], the valence neutrons seem

TABLE I. Properties of the monopole modes found in Ca isotopes at excitation energy ω. The 2qp decomposition (column transitions $\alpha \rightarrow \beta$), contribution to the strength $|X_{\alpha\beta}|^2 - |Y_{\alpha\beta}|^2$, and unperturbed energy $E_\beta + E_\alpha$, with E_μ the energy of the quasiparticle state μ, are displayed. The $|X|^2 - |Y|^2$ measure has been normalized such that $\sum_{\alpha\beta} |X_{\alpha\beta}|^2 - |Y_{\alpha\beta}|^2 = 1$. Transitions contributing less than 5% to the ISM strength are not reported.

Nucleus	ω (MeV)	Transition $\alpha \rightarrow \beta$	$E_\beta + E_\alpha$ (MeV)	$\lvert X_{\alpha\beta}\rvert^2 - \lvert Y_{\alpha\beta}\rvert^2$
^{50}Ca	12.8	$2p_{3/2} \rightarrow 3p_{3/2}$	14.2	0.4
^{60}Ca	12.6	$2p_{1/2} \rightarrow 3p_{1/2}$	12.4	0.34
		$2p_{3/2} \rightarrow 3p_{3/2}$	13.8	0.11
		$1f_{5/2} \rightarrow 2f_{5/2}$	14.2	0.05
^{62}Ca	4.3	$1g_{9/2} \rightarrow 1g_{9/2}$	2.6	0.30
		$2d_{5/2} \rightarrow 2d_{5/2}$	5.4	0.25
		$2s_{1/2} \rightarrow 2s_{1/2}$	5.3	0.19

to be decoupled from the protons, with neutron excitations extending over the whole volume of the nucleus. The proton contribution decreases with neutron excess, going from 15% for ^{50}Ca to less than 5% in the case of ^{62}Ca. The 4.3 MeV mode in ^{62}Ca, driven by pairing correlations, will be discussed in Sec. V.

B. Nickel isotopes

The previously discussed pattern of the emergence of low-energy resonances, with increasing isospin asymmetry, can also be tested in the nickel isotopic chain. The previously discussed pattern of the emergence of low-energy resonances, with increasing isospin asymmetry, can also be tested in the nickel isotopic chain. Figure 5 displays the monopole strength of $^{46-86}$Ni, obtained within the covariant QFAM. First focusing on the neutron-rich Ni isotopes, we expect new low-lying structures to emerge at $N = 30$ and $N = 52$, where orbitals that Fig. 5 displays show the monopole strength of $^{46-86}$Ni, obtained within the covariant QFAM. First focusing on the neutron-rich Ni isotopes, we expect new low-lying structures to emerge at $N = 30$ and $N = 52$, where orbitals that inaugurate new major shells start to be filled, i.e., the $2p_{3/2}$ and the $2d_{5/2}$ states, respectively. As illustrated in Fig. 6, filling the $2p_{3/2}$ to $1g_{9/2}$ orbitals yields resonances with energies around 18 MeV, while the occupation of the $2d_{5/2}$ and $3s_{1/2}$ states gives rise to monopole excitations around 11 MeV.

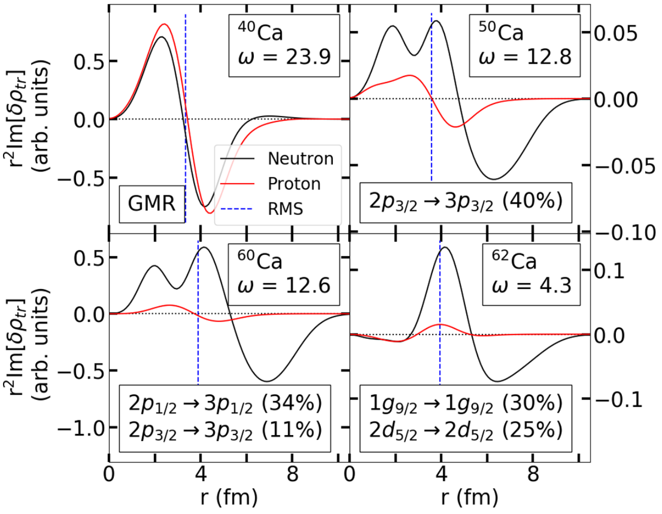

FIG. 4. Neutron (black) and proton (red) transition densities for ^{40,50,60,62}Ca. Excitation energies ω are given in MeV. The vertical blue line shows the ground-state rms matter radius of the nucleus.

To better understand the evolution of the monopole strength in the neutron-rich ^{58,68,79,80,86}Ni isotopes, Fig. 7 relates each low-energy mode with its dominant 2qp contributions, while Table II further details the energy gap between the two single-particle states of the transition, as well as the weight of the 2qp configuration. Hence, a new major shell, inaugurated by the $2p_{3/2}$ orbital, gets filled, going from ^{56}Ni to ^{58}Ni. Concomitantly, a new low-energy mode emerges at $\omega = 18.1$ MeV, dominated by the $2p_{3/2} \rightarrow 3p_{3/2}$ transition (42%; see Table II). Likewise, in ^{62,68,70}Ni, the occupation of the $2f_{5/2}$, $2p_{1/2}$, and $1g_{9/2}$ orbitals comes with new resonances, located at $\omega = 19.9$, $\omega = 15.6$, and $\omega = 18$ MeV, respectively. Their dominant 2qp contributions come from the $1f_{5/2} \rightarrow 2f_{5/2}$, $2p_{3/2} \rightarrow 3p_{3/2}$, and $1g_{9/2} \rightarrow 2g_{9/2}$ transitions, respectively. Adding more neutrons in the $2d_{5/2}$ and $3s_{1/2}$ orbitals opens a new major shell, and thus new peaks appear in ^{80,86}Ni at $\omega = 10.5$ and $\omega = 9.9$ MeV. Their dominant 2qp contributions come from the $2d_{5/2} \rightarrow 3d_{5/2}$ (32%) in the former, and are more evenly distributed between the $2d_{5/2} \rightarrow 3d_{5/2}$ (12%) and $3s_{1/2} \rightarrow 4s_{1/2}$ (14%) in the latter.

From a general point of view, the evolution of the monopole strength, in both Ca and Ni isotopic chains, is quite similar, mainly driven by the single-particle spectrum features. We have checked that these similarities are also present at the level of the transition densities. Interestingly, the low-energy part of the ^{68}Ni monopole strength is in agreement with the experimental results reported in Ref. [47], where a peak around 15 MeV is measured. Also, the structure of the strength obtained in $^{68-78}$Ni isotopes is in agreement with the calculations reported in Ref. [9], where the coupling to the continuum was considered. Therefore, this last effect does not impact the qualitative features of the monopole strength. However, it strongly impacts the width of the low-energy resonances and enhances their collectivity. Finally, the proton counterpart of low-energy modes can be observed in the neutron-deficient $^{46-56}$Ni (see Fig. 5) with the same mechanism of emergence. Decreasing the neutron number drives the proton Fermi energy towards the continuum, decorrelating protons that used to be bound, into a core in the case of the

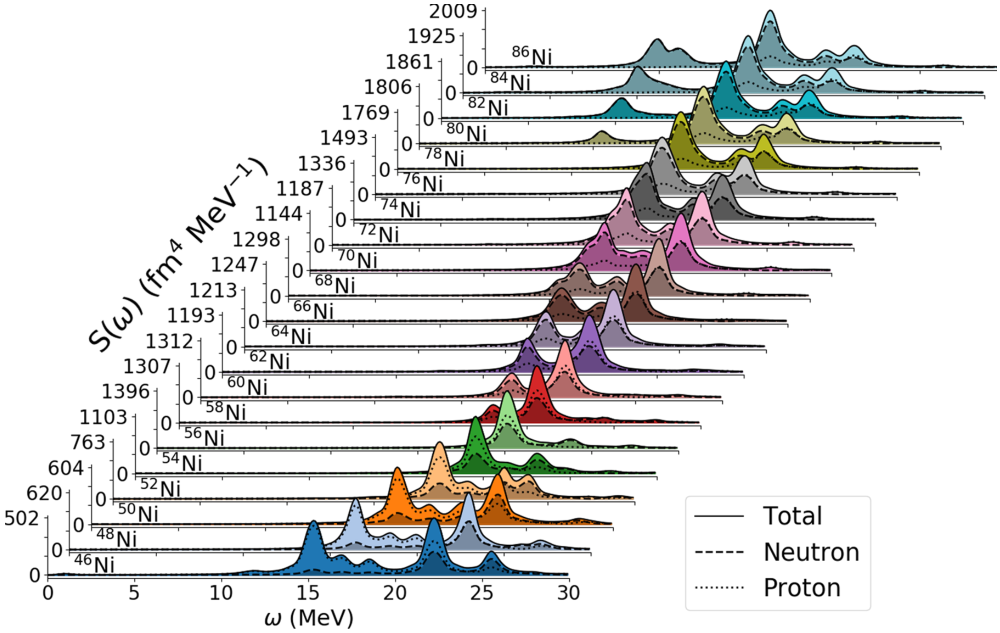

FIG. 5. Same as Fig. 2, but for Ni isotopes.

neutron-rich isotopes. As a result, the neutron contribution to the monopole strength between 15 and 20 MeV decreases, and new purely proton modes emerge, e.g., at $\omega = 15.5$ and $\omega = 17.3$ MeV in ^{46}Ni.

C. Soft modes contribution to the total strength

A possible way to quantify the evolution of soft modes with isospin asymmetry is to evaluate their global contribution to the total strength. For this purpose, Fig. 8 displays the evolution of the ratio of integrated strengths of the soft modes to the total one,

$$R \equiv \frac{\int_0^{\omega_{sm}} d\omega S(\omega)}{\int_0^{\omega_{tot}} d\omega S(\omega)}, \tag{15}$$

where ω_{sm} stands for the energy of the last soft mode, and $\omega_{tot} = 30$ MeV. The choice has been made here to use a nonenergy weighted sum rule in order to study in detail the low-energy excitations. This ratio is displayed for various isotopic chains, ranging from Ne to Ge. It should be noted that deformed nuclei have been constrained to a spherical shape, since it is relevant to keep the study of the impact of

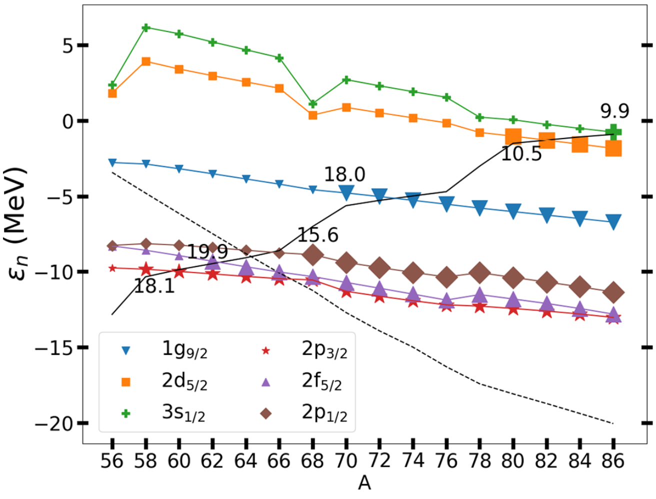

FIG. 6. Same as Fig. 3, but for Ni isotopes.

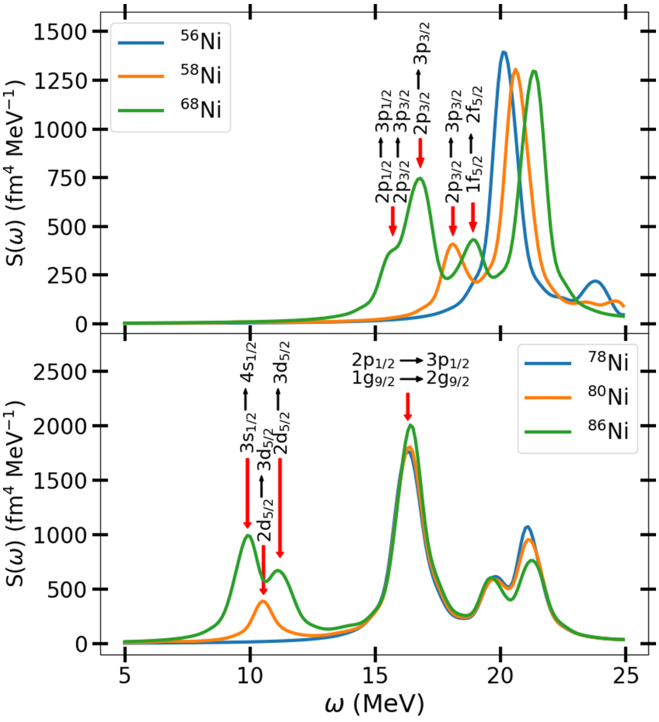

FIG. 7. Monopole strength of ^{56,58,68,79,80,86}Ni, with the main 2qp contributions indicated for the low-energy modes.

TABLE II. Same as Table I, for Ni isotopes.

Nucleus	ω (MeV)	Transition $\alpha \to \beta$	$E_\beta + E_\alpha$ (MeV)	$\lvert X_{\alpha\beta}\rvert^2 - \lvert Y_{\alpha\beta}\rvert^2$
^{58}Ni	18.1	$2p_{3/2} \to 3p_{3/2}$	16.0	0.42
		$2p_{1/2} \to 3p_{1/2}$	15.4	0.02
^{68}Ni	15.6	$2p_{1/2} \to 3p_{1/2}$	11.8	0.33
		$2p_{3/2} \to 3p_{3/2}$	10.0	0.13
^{70}Ni	18.0	$2p_{3/2} \to 3p_{3/2}$	7.0	0.22
		$1g_{9/2} \to 2g_{9/2}$	15.9	0.19
^{80}Ni	10.5	$2d_{5/2} \to 3d_{5/2}$	9.5	0.32
		$3s_{1/2} \to 4s_{1/2}$	9.0	0.06
		$2d_{3/2} \to 3d_{3/2}$	9.1	0.04
^{86}Ni	9.9	$3s_{1/2} \to 4s_{1/2}$	8.4	0.14
		$2d_{3/2} \to 3d_{3/2}$	8.0	0.12

deformation, for the next section. When there are multiple soft modes, separated by few MeV, the sum of the soft modes up to the last one is considered.

The general trend corresponds to a systematic increase of the proportion of the soft mode in the total monopole strength with neutron excess. This ratio can reach close to 80% of the total strength for nickel, iron, or sulfur in very neutron-rich nuclei. Here again, the relation between the opening of a major shell and the emergence of soft neutron modes is visible, i.e., adding neutrons on top of configurations with $N = 14, 28, 50$ yields a sudden increase of the contribution of soft modes. On the other hand, adding neutrons on top of the $N = 20$ shell closure has little impact, although an inflexion in the evolution of the soft modes' proportion can be observed in a sulfur and neon isotopic chain (Fig. 8). In the case of argon and calcium isotopes, the mismatch between the proton and neutron Fermi energies is not large enough to trigger a low-energy resonance at $N = 22$.

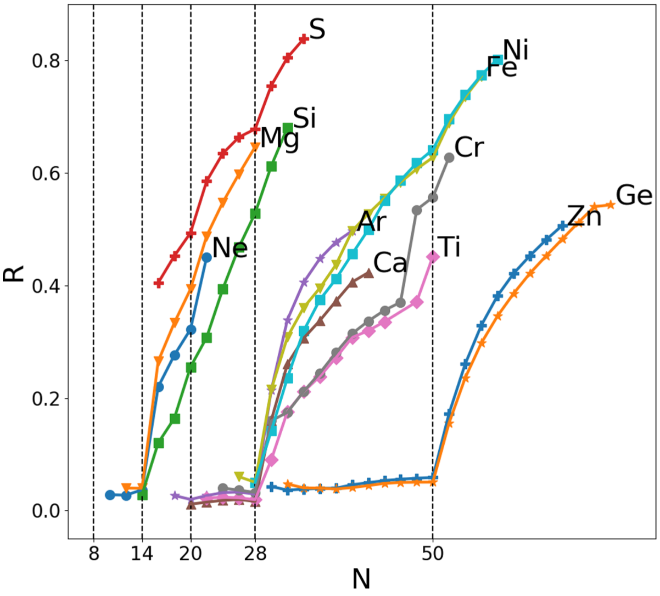

FIG. 8. Evolution of the ratio (15), with the neutron number N, for various isotopic chains. The integration over soft neutron modes is performed up to $\omega_{sm} \approx$14–18 MeV, depending on the position of the GR for each nuclei.

Another feature is that substructures stemming from the opening of subshells have negligible effects in the evolution of this ratio: when the occupation of an orbital opens a new possible monopole transition, the studied ratio is not impacted. However, one exception occurs with the $2s_{1/2}$ orbital: its filling gives rise to the first appearance of a neutron soft mode in neon, magnesium, silicone, and sulfur at $N = 16$. This may be related to the fact that $N = 14$ is a strong subshell closure [48].

Finally, it is relevant to compare these results to the ones previously obtained in the case of isovector dipole (IVD) excitation, where a similar low-energy pattern has also been identified. In the case of IVD resonance, it is possible to interpret the fraction of strength carried by the soft modes in terms of low- and high-l orbitals filling [24]. In particular, between $N = 34$ and 50, where high-l orbitals are filled, we have checked that there is no sharp increase of the strength fraction due to the low-energy mode. However, in the present case of ISM, such an effect is not visible and, hence, an interpretation in terms of low- and high-l orbital filling does not seem to apply.

IV. EVOLUTION OF LOW-ENERGY ISOSCALAR MONOPOLE MODES WITH DEFORMATION

We now wish to investigate the impact of deformation on the structure of the low-energy part of the monopole strength. The splitting of these modes, with the onset of deformation, is a known feature in different multipolarities both experimentally and theoretically [49–52]. The role played by deformation, in the appearance of so-called cluster modes at very low energy, was also studied in detail in $N = Z$ nuclei [14]. The aim of this section is to extend the analysis to neutron-rich systems. In order to assess how nuclear deformation affects the structure of the monopole strength, we performed QFAM calculations on top of RHB reference states, constrained to different axial deformations, parametrized by the axial quadrupole parameter $\beta_2 \in [-0.2, 0.8]$ on the total neutron + proton density. This allows one to monitor the various monopole resonances as the deformation of the system is changed, both for soft and

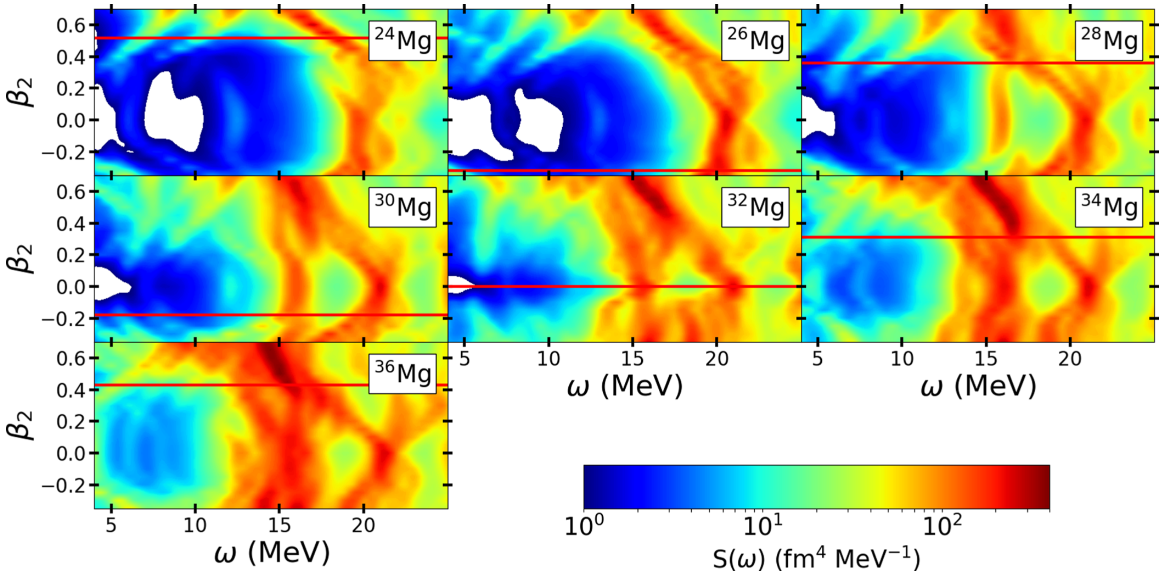

FIG. 9. Evolution of the monopole strength distribution, in Mg isotopes, with the deformation of the reference RHB state, on top of which the QRPA response is built. The red lines show the ground-state deformation for each nuclei at the RHB level.

cluster modes, each of them addressed separately in the next two sections.

A. Evolution of soft modes with deformation and neutron excess

The evolution of soft modes with deformation, and isospin asymmetry, involves generic patterns, which will be illustrated in the specific case of Mg isotopes. We start by examining the evolution of the monopole strength in Mg isotopes as the constrained axial quadrupole deformation of the RHB reference state varies from $\beta_2 = -0.2$ to $\beta_2 = +0.8$ (Fig. 9). The evolution of the monopole strength with neutron excess, in spherically constrained Mg isotopes ($\beta_2 = 0$ slice in each panel of Fig. 9), is in agreement with the previous discussion on the emergence of neutron low-energy modes. Namely, a low-energy mode appears in ^{28}Mg, related to the filling of the $2s_{1/2}$ orbitals. Then, the width of the strength increases in ^{30}Mg due to an additional excitation from $1d_{3/2}$ to $2d_{3/2}$. In ^{34,36}Mg, a new soft mode at $\omega \approx 13.5$ MeV emerges, stemming from the filling of the $1f_{7/2}$ orbital.

The impact of deformation in the low-energy part of the monopole strength can be studied by tracking the soft modes as the deformation switches on, and increases. Focusing on ^{32}Mg (see the corresponding panel in Fig. 9 as well as in Fig. 10), the onset of deformation causes a splitting of the soft modes, similarly to what is known for the GMR. For instance,

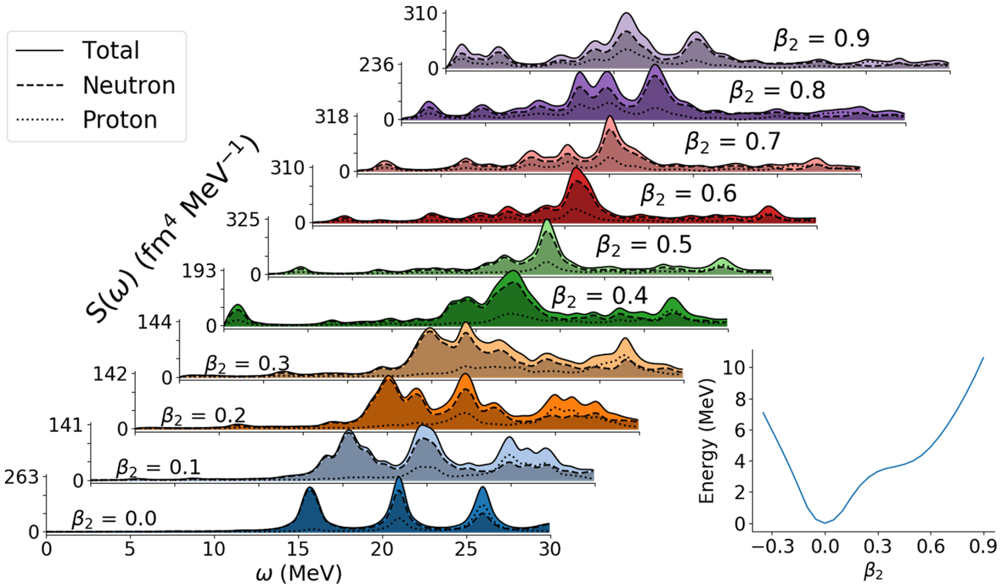

FIG. 10. Left: evolution of ^{32}Mg monopole strength distribution with the deformation of the reference RHB state, split into total (solid line), neutron (dashed line), and proton (dotted line) contributions. Right: total energy curve of ^{32}Mg, with respect to the axial quadrupole deformation parameter β_2.

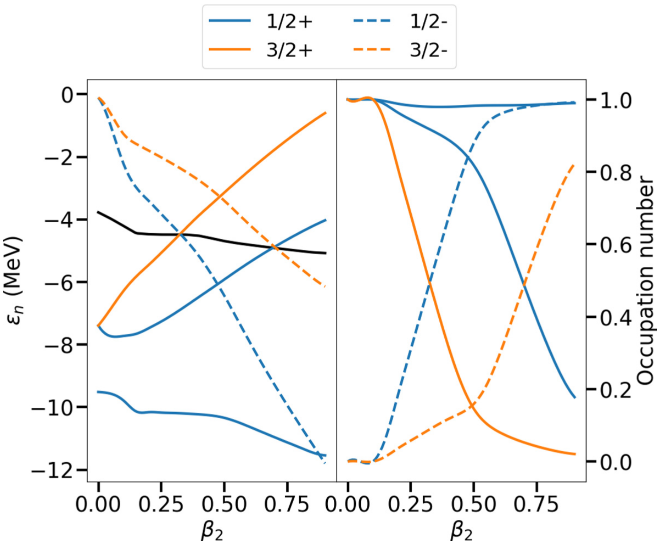

FIG. 11. Subset of ^{32}Mg neutron canonical single-particle energies (left) and their occupation number (right), plotted against the axial quadrupole deformation parameter β_2. The black line shows the neutron Fermi level.

the resonance found at $\omega = 15.5$ MeV, in the spherical ^{32}Mg, splits into four components in the deformed $\beta_2 = 0.1$ case, located at $\omega = 14.0$, 15.4, 16.5, and 17.5 MeV, respectively. A fifth component is visible at $\omega \approx 11.8$ MeV, the latter acquiring more strength as the deformation increases.

Because of the noncollective nature of these soft modes, one can draw a correspondence between the splitting in the strength and the splitting induced by the axial deformation at the level of the canonical single-particle spectrum (Fig. 11). For instance, the dominant 2qp contributions of the 15.7 MeV monopole mode of ^{32}Mg, at $\beta_2 = 0$ (see Fig. 10), are $2s_{1/2} \rightarrow 3s_{1/2}$ and $1d_{3/2} \rightarrow 2d_{3/2}$. With the onset of deformation, the spherical $1d_{3/2}$ orbital splits into nondegenerate $\Omega^\pi = 1/2^+$ and $\Omega^\pi = 3/2^+$ states, where Ω stands for the projection of the total angular momentum J on the symmetry axis [chosen to be the (Oz) axis] and π the parity of the state. With the breaking of the rotational symmetry, these states do not belong to an irreducible representation of the SU(2) group labeled by the eigenvalues of J^2, but rather mix the $m = \Omega$ component of positive parity spherical orbitals (provided reflection symmetry remains unbroken): the $\Omega^\pi = 1/2^+$ axially symmetric state results from the mixing of the $m = 1/2$ component of the s, d, g, etc. orbitals.

In ^{32}Mg, as the $1d_{3/2}$ orbital splits into a $\Omega^\pi = 1/2^+$ state and a $\Omega^\pi = 3/2^+$ state, new transitions take place between the occupied $1/2^+$ ($3/2^+$) and all the other unoccupied $1/2^+$ ($3/2^+$) begotten by the SU(2) symmetry breaking. Therefore, many more transitions are available, as compared to the spherical case, causing an enhancement of the collectivity of the low-energy resonances. For instance, in the case of ^{32}Mg at $\beta_2 = 0.1$, between $\omega = 11$ and $\omega = 16$ MeV, almost 10 transitions are involved and carry a non-negligible part of the strength (more than 5% of the total strength each). In appears that what is called a monopole mode, in such a deformed framework, should be understood as a mixing between monopole, quadrupole, etc. transitions.

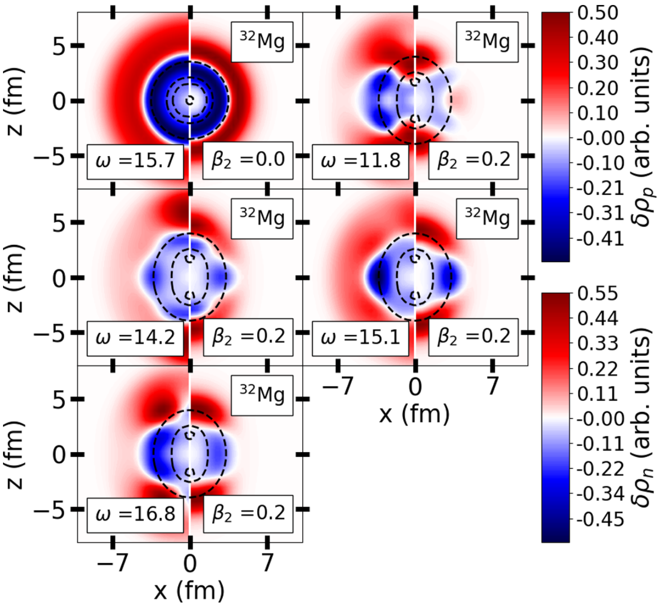

FIG. 12. Neutron (left part of each panel) and proton (right part of each panel) transition densities, associated to resonances with excitation energy ω (in MeV) of ^{32}Mg constrained at deformation β_2. The black dashed lines show the contour of the unperturbed total density (solution of the static, constrained RHB equation) around which the nucleus vibrates.

In the case of a larger deformation, Fig. 10 shows that the GMR is shifted to lower energy, as expected, and starts to merge with the soft modes. However, the distinction between soft modes, and GMR, can be made by looking to the proton contribution to the total strength (dotted lines in Fig. 10). When the latter is nonzero, there is a coherent excitation of both protons and neutrons, corresponding to the GMR. Based on these criteria, we deduce that the soft modes vanish for $\beta_2 > 0.7$ due to the spreading of the GMR (Fig. 10).

Transition densities are shown in Fig. 12 for the mode located at $\omega = 15.7$ MeV in the spherical ^{32}Mg, as well as for the modes at $\omega = 11.8$, 14.2, 15.1, 16.8 MeV in ^{32}Mg, constrained to $\beta_2 = 0.2$. Deformation generates localization on the transition densities, as shown by the proton one in the core of the nucleus, and the neutron one both in the core and in the surface of ^{32}Mg.

The spatial properties of the transition densities, shown in Fig. 12, can be further analyzed in terms of the 2qp contributions to the corresponding modes, and of the shape of the canonical orbitals, involved in the corresponding monopole transitions. The first column of Fig. 13 corresponds to the monopole mode at $\omega = 15.7$ MeV, in the spherical ^{32}Mg. It displays the canonical states participating in the dominant 2qp configuration, i.e., the 2 and $3s_{1/2}$ orbitals, as well as the 1 and $2d_{3/2}$ orbitals. The corresponding configurations contribute about 50% to the monopole strength. The second column of Fig. 13 corresponds to the excitation at $\omega = 11.8$ MeV in ^{32}Mg, constrained at $\beta_2 = 0.2$. The main 2qp contribution to this mode involves the 1/2+(4) state, which coincides with

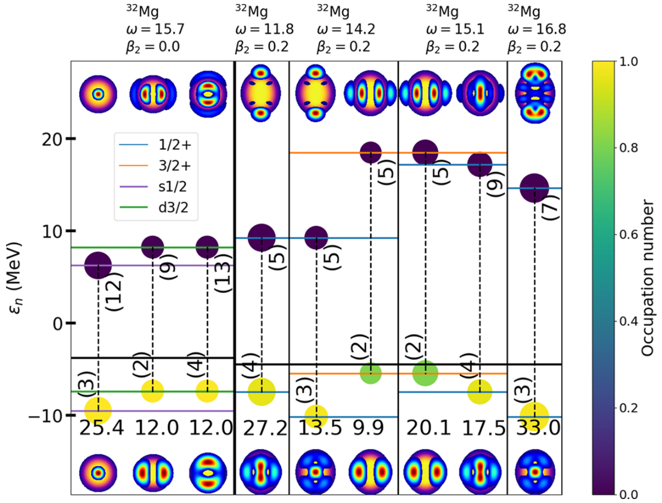

FIG. 13. Canonical neutron orbitals, involved in the dominant monopole transitions contributing to the modes found at excitation energy ω (in MeV) in ^{32}Mg, with axial quadrupole deformation β_2. The percentage which the transition contributes to the monopole strength is indicated by the number and the surface area of the circle on top of the level, with a color giving the occupation number of the orbital. The number in parentheses shows the principal quantum number of each level. Partial densities of the orbitals, involved in the monopole transitions, are plotted on top of the total nucleon density.

the $m = 1/2$ component of the $1d_{3/2}$ in the $\beta_2 = 0$ limit. Here, only some features of the transition density can be related to the 2qp configuration, namely, the localization of the neutron transition density on the radial axis, visible on the fourth $1/2+$ orbital. It should be noted that one cannot expect a full correspondence between the main 2qp configurations and the transition densities since the contribution of the former is about 30%.

The third and fourth columns of Fig. 13 correspond to the $\omega = 14.2$ and $\omega = 15.1$ MeV monopole modes, found in ^{32}Mg constrained at $\beta_2 = 0.2$. Both modes are slightly more collective than the ones located at $\omega = 11.8$ and $\omega = 16.8$ MeV. The major 2qp contribution to the resonance located at 14.2 MeV comes from the $1/2+(3) \rightarrow 1/2+(5)$ transition, where the $1/2+(3)$ state coincides with the $2s_{1/2}$ orbital, in the $\beta_2 = 0$ limit. In this case again, the shape of the partial densities associated to this sole transition allows one to understand the main spatial properties of the corresponding transition density in Fig. 12, and to interpret this mode as a cluster vibration. On the other hand, the excitation found at $\omega = 15.1$ MeV is dominated by the $3/2+(2) \rightarrow 3/2+(5)$ transition, where the $3/2+(2)$ state coincides with the $m = 3/2$ component of the $1d_{3/2}$ orbital in the $\beta_2 = 0$ limit, together with a contribution coming from the $1/2+(4) \rightarrow 1/2+(9)$ transition. In that case also, one can trace back the spatial properties of the corresponding neutron transition density (Fig. 12), namely, a pronounced contribution on the horizontal axis, to the shape of the canonical partial densities. Finally, the last column of Fig. 13 shows the mode at $\omega = 16.8$ MeV, where the state matching the 1/2 component of the $2s_{1/2}$, in the $\beta_2 \rightarrow 0$ limit, is involved. The main corresponding 2qp contribution comes from the $1/2+(3) \rightarrow 1/2+(7)$ transition, with again a shape of the transition density, which can be understood by looking at the canonical partial densities.

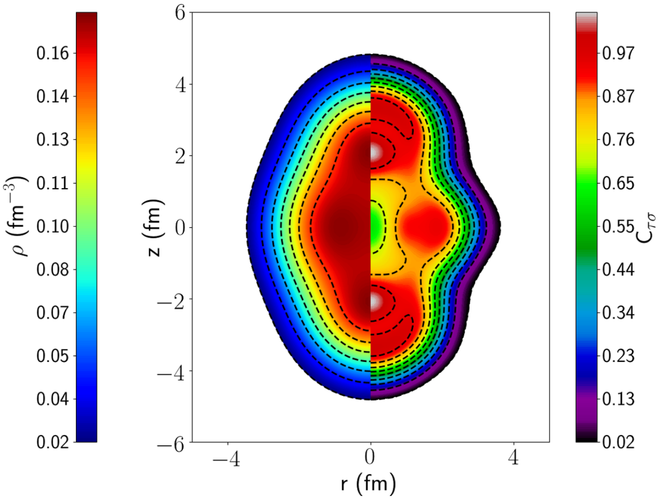

FIG. 14. Ground-state density (left) and localization function (right) of ^{20}Ne.

B. Evolution of cluster excitation with deformation and neutron excess

Cluster vibrations, described as coherent excitation of neutrons and protons localized in clusters, are expected to occur in $N = Z$ nuclei at low energies—typically between 5 and 10 MeV—and large deformations [14]. In this section, we investigate the impact of neutron excess on these modes.

In order to study cluster excitations, it is relevant to explain how they could be traced. Figure 14 displays the ground-state density and localization function of ^{20}Ne, where cluster structures can be identified, while Fig. 15 shows the transition density in a so-called cluster mode (on the left), compared to the one of the GMR (on the right), located at larger energy. In the case of the low-energy mode, the main contribution to the excitation is located close to the clusters ones and in the core of the nucleus, which can be interpreted as a cluster oscillation with respect to the core. In the case of the GMR transition density, the clusters, located in the surface of the nucleus, also contribute to the excitation, but at the same time, deplete the core, which corresponds to the usual breathing mode. Therefore, in the same way that a broad neutron contribution far from the core, in the transition density of neutron rich nuclei, is interpreted as a neutron skin oscillation, the spatial excitation patterns of the transition density in Fig. 15 here is interpreted as a cluster vibration, namely, a large contribution to the vibration from the cluster, oscillating against the core. It should be noted that during the excitation, the clusters partially merge with the core. Hence this mode does not represent a proper oscillation of cluster against a core, but a more complex pattern. However, in the present work, we define such modes as cluster vibration and cluster oscillation, which, of course, remains subjective.

For all the Mg isotopes considered in Fig. 9, there is a systematic occurrence of low-energy modes, starting from

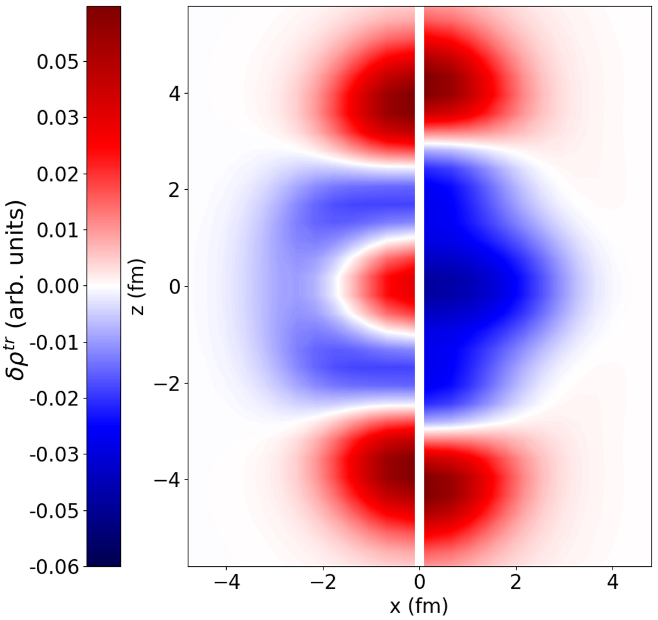

FIG. 15. Comparison between transition densities at $\hbar\omega = 6.75$ MeV corresponding to the cluster region (left panel) and $\hbar\omega = 17.9$ MeV corresponding to the GMR region (right panel) of ^{20}Ne under ISM excitation.

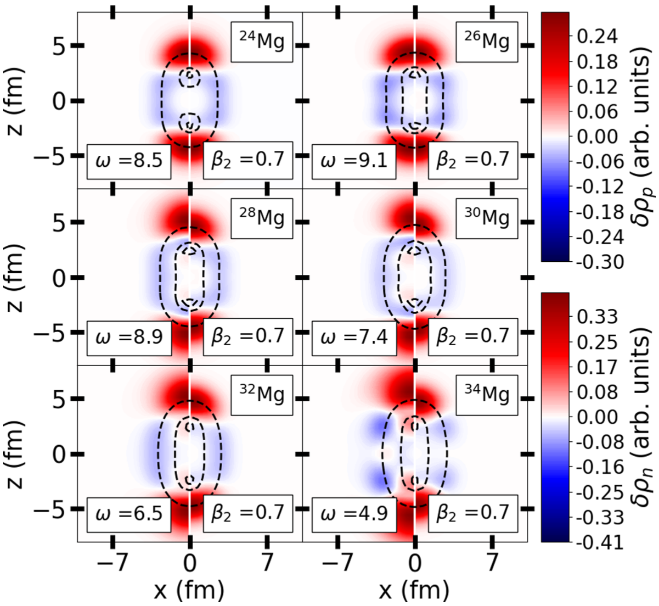

FIG. 16. Transition densities for some magnesium isotopes. Excitation energies are given in MeV. Deformation is constrained to take the value of $\beta_2 = 0.7$ for all nuclei. On the left of each plot is shown the neutron density, and on the right the proton one. The dashed black lines represent the rms radius for the matter ground state as well as the maximum of density in the ground state to emphasize the cluster structure.

$\beta_2 \approx 0.4$. The analysis of these modes, in terms of 2qp configurations, and the computation of the time-dependent density, allows one to tag them as cluster oscillations. Let us focus again on one typical example, from ^{32}Mg. In Fig. 10, a new structure in the monopole strength starts to develop around $\omega = 6$ MeV, from $\beta_2 \approx 0.2$, and increases with deformation. The emergence of this mode can be traced back to the shell structure of ^{32}Mg in Fig. 11: the 1/2-(3) and 3/2-(2) states, responsible for localizing neutrons in clusters along the symmetry axis, quickly fall towards the Fermi energy as the quadrupole deformation increases. They even become fully occupied from $\beta_2 \approx 0.4$ for the former and $\beta_2 \approx 0.7$ for the latter (see, also, the corresponding occupation numbers plotted against β_2 in the right panel of Fig. 10). As for proton orbitals, the dominant transitions contributing to the mode at $\omega \approx 6$ MeV are the same for all Mg isotopes, namely, 1/2+(2)→1/2+(3), 1/2-(2)→ 1/2-(3), and 3/2+(1)→3/2+(3). Again, these levels are the ones localizing the protons in clusterized structures along the symmetry axis.

In order to understand the interplay between deformation and neutron excess in cluster modes, the transition densities of these modes in $^{24-32}$Mg isotopes are displayed in Fig. 16. The cluster structure, which can be interpreted as a ^{12}C + ^{12}C oscillation in the excited state, can be seen on the transition densities of ^{24}Mg, where the neutron and proton oscillate in phase, in the cluster's location. However, even if the cluster structure is clear, this interpretation in terms of ^{12}C + ^{12}C oscillation remains a conjecture, and a more in-depth work would be needed to determine the exact nature of the clusters, especially the behavior of the density of the core. To emphasize the use of "cluster vibration," it is important to notice that the contribution of the transition densities is mainly located in the poles where preformed clusters are present, meaning that mainly the cluster structure will be impacted during the excitation. This feature can be seen in Fig. 16, where the ground-state densities are shown by a dashed line.

When the neutron number increases, the neutron and proton transition densities get slightly shifted with respect to each other, but the main effect occurs closer to the center of the nucleus: additional peaks appear in the neutron transition density. This implies more complex vibrations than a mere oscillation of the clusters, namely, small additional contributions to the excitation, mainly at an average distance between the center and the surface of the nucleus, on the symmetry axis. However, it should be noted that the ^{12}C + ^{12}C oscillation is still present in all the considered isotopes.

V. EVOLUTION OF LOW-ENERGY ISOSCALAR MONOPOLE MODES WITH PAIRING

As mentioned in the case of ^{62}Ca, another kind of low-energy mode appears below 5 MeV, driven by pairing correlations. Such excitations have been discussed both theoretically and experimentally; see, e.g., [53–55]. Pairing vibration modes refers to coherent excitations involving particle-particle, particle-hole, and hole-hole contributions. Their properties were analyzed within the QRPA framework both for spherical [56–58] and deformed [59] nuclei. In the present work, we investigate the possible interplay between pairing and cluster modes.

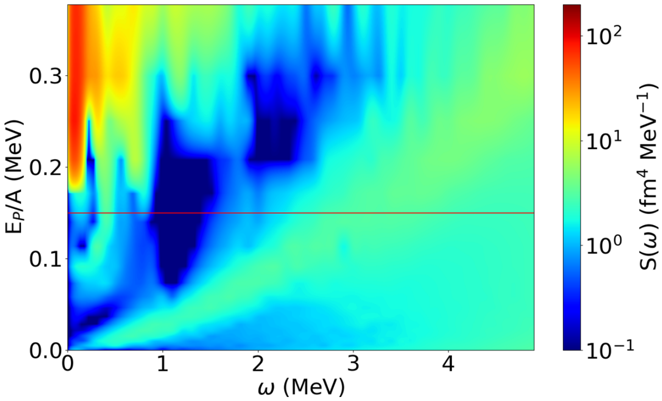

FIG. 17. Evolution of the monopole strength function of ^{54}Ca with the pairing energy of the RHB level. The red horizontal line shows the pairing energy of the ground-state ^{54}Ca.

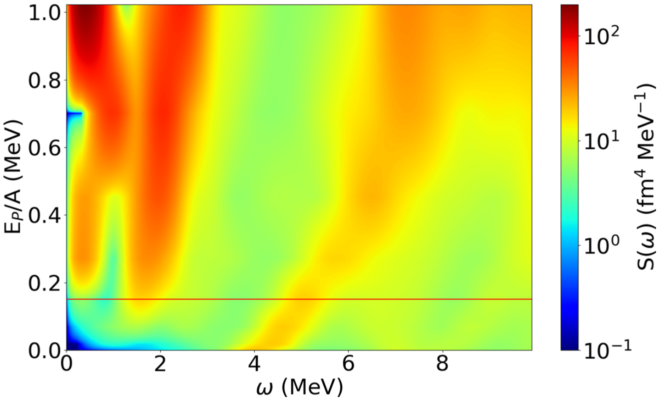

FIG. 18. Evolution of the monopole strength function of ^{34}Mg with the pairing energy of the RHB level. The deformation is fixed to $\beta_2 = 0.31$ which is the ground-state (GS) deformation of this nucleus. The red horizontal line shows the pairing energy of the ground-state ^{34}Mg.

A. Spherical case

How pairing correlations influence the monopole strength distribution can be studied along the same lines as in the deformed case, i.e., by constraining the amount of pairing correlation captured by the reference RHB state and then monitoring the monopole strength as pairing correlations increase. Following Ref. [60], the constraint on pairing is implemented by varying the strength of the pairing interaction, from 0 to twice its normal value, both at the RHB and QFAM levels. We define the total pairing energy per nucleon (E_{pair}/A) as an acceptable order parameter for the normal to superfluid phase transition and plot our result against the latter.

We first focus on the evolution of the ISM strength distribution with pairing correlation at zero deformation. As soon as the pairing energy reaches a threshold value, the last occupied orbitals will start to deplete, enabling low-energy pair excitations.

This typical behavior is illustrated in the case of ^{54}Ca. Figure 17 shows the evolution of the ISM strength function with the pairing energy per nucleon associated to the RHB reference state (the total pairing energy in the RHB ground state being 7.6 MeV). With the increase of pairing correlations, a new mode appears below 1 MeV, stemming from the fact that the $2p_{1/2}$ orbital becomes partially occupied. This mode already appears in ^{54}Ca ISM strength built on top of the RHB ground state, however with a negligible contribution: the maximum strength of ^{54}Ca, corresponding to the GMR, is $\approx$600 fm^4 MeV^{-1}, while this low-energy mode has a peak of only $\approx$5 fm^4 MeV^{-1}. For large pairing correlations, this excitation carries more strength, up to $\approx$100 fm^4 MeV^{-1} within the range considered for the constrained calculations.

This typical behavior is quite general and has been checked for several nuclei, both in the calcium and nickel isotopic chains. The contribution of pairing-type excitations to the total ISM strength remains very low, but increases if the pairing is constrained to larger values. The typical excitation energy range depends on the pairing energy since this resonance can be considered as a pure pairing mode: the energy of the excitation is then expected to be of the order of $\approx 2\Delta$, where Δ stands for the pairing gap, explaining why the excitation energy of the pairing mode increases with the pairing energy itself. A typical transition density is plotted in Fig. 4 in the bottom right corner for ^{62}Ca. The corresponding state is also visible on the strength of ^{62}Ca in Fig. 2. While the proton contribution is negligible, the neutron part displays a behavior similar to what was observed for pure neutron modes at higher energy, i.e., a very broad neutron skin oscillation.

B. Deformed case

The appearance of a very low-energy pairing mode in deformed and neutron-rich nuclei was already discussed in Ref. [59] for quadrupole excitations. In the case of monopole excitations in deformed nuclei, a mixing with the quadrupole modes is expected and shall lead to similar results. Since the onset of pairing correlations is likely to reduce the amount of deformation, the latter is fixed during the calculation in order to focus on the effect of pairing only, in the presence of clusterized structures.

Taking ^{34}Mg as a representative of both deformed and superfluid light nuclei, Fig. 18 displays the evolution of the corresponding ISM strength distribution with the amount of pairing correlations captured by the RHB reference state, with a quadrupole deformation parameter fixed to the ground-state value ($\beta_2 = 0.31$). It has to be remembered here that a subtraction of the spurious states is performed and can impact the very low-energy part of the strength since numerical subtractions are never perfect. However, our results on the low-energy pairing resonances in the monopole channel are in agreement with results of Ref. [29]. Since this last approach is somewhat different from ours (for instance, QRPA vs QFAM or covariant EDF vs Skyrme), this may suggest that the present numerical uncertainties, related to the subtraction scheme, remain negligible.

At zero pairing energy, a few peaks are already visible, mainly around 4 MeV. This excitation corresponds to the previously studied cluster excitation, where proton and neutrons behave coherently, generating a cluster oscillation around a

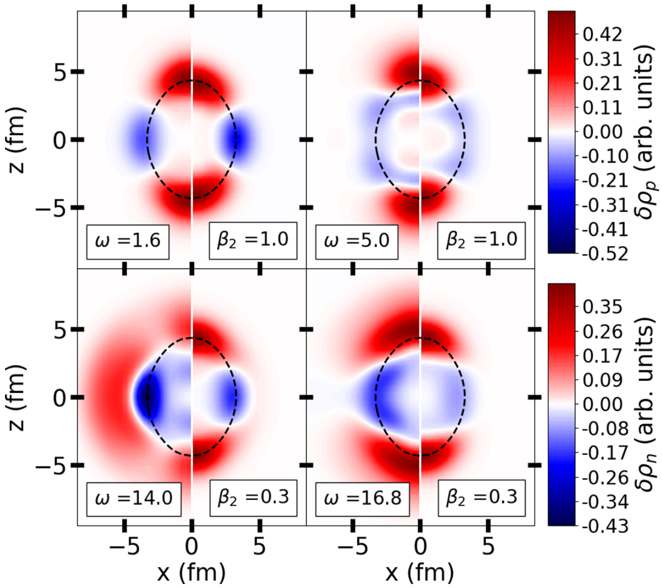

FIG. 19. Same as Fig. 16, but for ^{34}Mg. Excitation energy ω are given in MeV. The top left plot corresponds to a pairing excitation, and the top right one to a cluster excitation. The bottom left is a pure neutron mode and the bottom right is a GR mode.

core. Two other cluster excitations, at 7 and 9 MeV, carry much less strength and are barely visible in the figure.

Increasing the pairing energy triggers new resonances at very low energy, below 2 MeV. They correspond to pure pair excitation. Interestingly, these transitions involve both protons and neutrons. A calculation of the free response (without the residual interaction) shows that the proton strength, at these very low energies, is negligible. Hence, the residual interaction plays an important role for the pair excitation in neutron-rich nuclei by involving protons. However, this is not a generic property since, for a calcium isotopic chain, for instance, no contribution from protons to the strength was found.

In the case of ^{34}Mg, the origin of these excitations can be traced back to different orbitals, depending on the pairing intensity. For a total pairing energy below 10 MeV, the low-energy excitations are dominated by the 3/2+(2) and 1/2-(3) single-particle states for neutrons, and the 3/2+(1) single-particle state for protons. For larger pairing energies, the neutron contribution to the pairing modes is dominated by the 1/2-(3) and 3/2-(2) orbitals, while the proton contribution is dominated by the 3/2+(1) and 1/2+(2) orbitals.

The transition densities of low-energy monopole modes in ^{34}Mg are displayed in Fig. 19. Neutrons and protons contribute similarly to the transition density for the two lowest-energy modes, i.e., the pairing ($\omega = 1.6$ MeV) and the cluster ($\omega = 5$ MeV) modes, whereas neutrons dominate the transition density in the $\omega = 14$ and $\omega = 16.8$ MeV modes, corresponding to the GMR and its low-energy tail.

As for the interplay between pairing and cluster modes, we observe a modification of the structure of the cluster excitation (located at $\omega = 5$ MeV in the unconstrained ISM strength) as pairing correlation gets stronger. From the decomposition of the cluster mode into its 2qp component, we observe a transition between a mixture of particle-hole transitions and pair excitation to a pure pair excitation, which dominates because of the partial depletion of the occupied orbitals near the Fermi level.

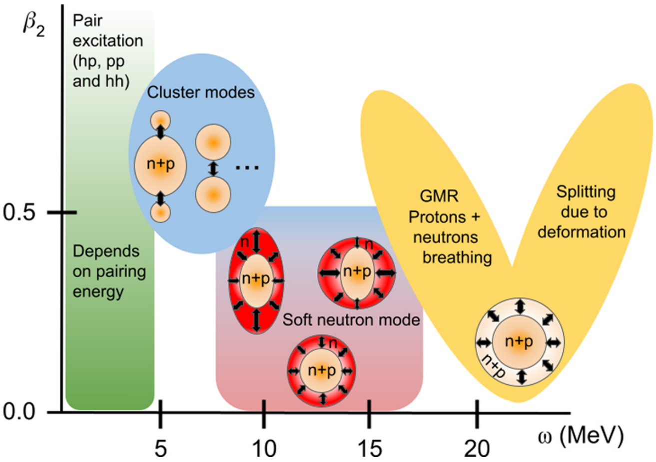

FIG. 20. Schematic view of a typical ISM strength landscape for low mass nuclei ($N < 120$). See the main text for more details.

VI. CONCLUSION

A systematic analysis of the low-lying ISM strength distribution in neon to germanium isotopic chains, and especially of the interplay between isospin asymmetry, deformation, and superfluidity, was performed within a microscopic approach, namely, the covariant quasiparticle finite amplitude method. The nature and characteristics of the encountered monopole resonances are sketched in Fig. 20.

Neutron-rich systems feature pure neutron low-energy modes, usually located between 5 and 15 MeV. A detailed analysis of these modes in terms of 2qp contributions showed that they are built from a single or a couple of single-particle configurations. This is explained by shell opening effects due to neutron excess. In particular, it has been shown that magic numbers play an important role: adding two neutrons on top of a magic core shall lead to the appearance of a new peak at low energy in the monopole strength. The additional appearance of peaks can occur due to subshell opening. The collective nature of the corresponding excitation depends on the number of levels involved in a major shell. These soft neutron modes exhibit a neutron skin, which has been successfully interpreted in terms of the canonical densities involved in the excitation. However, the effect of the coupling to the continuum might change the quantitative results presented here by increasing the width of the different low-energy resonances. A proper treatment of this coupling would be needed to obtain more reliable results. Similarly, taking into account the couplings is expected to quantitatively modify the results presented here, although the conclusions remain very similar [7].

The impact of deformation has been studied by constraining the value quadrupole parameter β_{20} over a significant range. This method allows for a better understanding of the evolution of the different excitations with the deformation. In particular, the soft neutron mode remains stable with deformation in most of the cases, and mixes with the GR around $\beta_2 = 0.3$, due to the shift of the GR to lower energy, with deformation. Splittings of these soft modes are also visible and were interpreted as additional excitations, allowed by shell opening, due to the deformation. Different modes were studied and two classes of excitations coexist: a mode corresponding to an oscillation along the deformation axis and another one to an oscillation perpendicular to this one. Evolving toward very large deformations destroys the soft neutron mode and favors the cluster ones. It should be noted that the above-defined "cluster vibration and oscillation" remain subjective definitions and the behavior of the clusters with respect to the core of the nuclei is still to be determined with a more in-depth study.

Finally, pair excitations also emerge below 5 MeV and correspond to excitation mixing pp, ph, and hh channels, inside a single level. These kinds of transitions are possible thanks to pairing, which can modify occupation numbers, allowing for partly occupied levels. The energy related to such an excitation would be $\approx\Delta$, where Δ refers to the pairing gap. A mixing between pairing and cluster excitations is predicted, with the latter transforming into the former with increasing pairing effects. However, since pairing and deformation are generally competing effects, it is unlikely to find both significant cluster and pairing modes in the same nucleus. All these results show that the low-energy spectrum of the monopole strength exhibits a rather complex and specific behavior with respect to neutron excess, deformation, and pairing.

---

[1] N. Paar, D. Vretenar, E. Khan, and G. Colò, Rep. Prog. Phys. **70**, R02 (2007).

[2] D. Savran, T. Aumann, and A. Zilges, Prog. Part. Nucl. Phys. **70**, 210 (2013).

[3] A. Bracco, E. G. Lanza, and A. Tamii, Prog. Part. Nucl. Phys. **106**, 360 (2019).

[4] E. Khan, N. Paar, and D. Vretenar, Phys. Rev. C **84**, 051301(R) (2011).

[5] J. C. Pei, M. Kortelainen, Y. N. Zhang, and F. R. Xu, Phys. Rev. C **90**, 051304(R) (2014).

[6] J. Piekarewicz, Phys. Rev. C **96**, 044314 (2017).

[7] D. Gambacurta, M. Grasso, and O. Sorlin, Phys. Rev. C **100**, 014317 (2019).

[8] E. Yüksel, E. Khan, and K. Bozkurt, Eur. Phys. J. A **49**, 124 (2013).

[9] I. Hamamoto and H. Sagawa, Phys. Rev. C **90**, 031302(R) (2014).

[10] Y. Chiba and M. Kimura, Phys. Rev. C **91**, 061302(R) (2015).

[11] Y. Chiba, M. Kimura, and Y. Taniguchi, Phys. Rev. C **93**, 034319 (2016).

[12] Y. Kanada-En'yo, Phys. Rev. C **93**, 054307 (2016).

[13] Y. Kanada-En'yo and K. Ogata, Phys. Rev. C **101**, 014317 (2020).

[14] F. Mercier, A. Bjelčić, T. Nikšić, J.-P. Ebran, E. Khan, and D. Vretenar, Phys. Rev. C **103**, 024303 (2021).

[15] G. Kühner, D. Meuer, S. Müller, A. Richter, E. Spamer, O. Titze, and W. Knüpfer, Phys. Lett. B **104**, 189 (1981).

[16] R. D. Starr, P. Axel, and L. S. Cardman, Phys. Rev. C **25**, 780 (1982).

[17] Z. W. Bell, L. S. Cardman, and P. Axel, Phys. Rev. C **25**, 791 (1982).

[18] P. G. Hansen and B. Johnson, Europhys. Lett. **4**, 409 (1987).

[19] T. Kobayashi, S. Shimoura, I. Tanihata, K. Katori, K. Matsuta, T. Minamisono, K. Sugimoto, W. Müller, D. L. Olson, T. J. M. Symons, and H. Wieman, Nucl. Phys. B **232**, 51 (1989).

[20] T. Aumann *et al.*, Nucl. Phys. A **649**, 297 (1999).

[21] D. Vretenar, N. Paar, P. Ring, and G. A. Lalazissis, Phys. Rev. C **63**, 047301 (2001).

[22] J. Terasaki, J. Engel, M. Bender, J. Dobaczewski, W. Nazarewicz, and M. Stoitsov, Phys. Rev. C **71**, 034310 (2005).

[23] N. Paar, Y. F. Niu, D. Vretenar, and J. Meng, Phys. Rev. Lett. **103**, 032502 (2009).

[24] T. Inakura, T. Nakatsukasa, and K. Yabana, Phys. Rev. C **84**, 021302(R) (2011).

[25] N. Ryezayeva, T. Hartmann, Y. Kalmykov, H. Lenske, P. von Neumann-Cosel, V. Yu. Ponomarev, A. Richter, A. Shevchenko, S. Volz, and J. Wambach, Phys. Rev. Lett. **89**, 272502 (2002).

[26] N. Tsoneva, H. Lenske, and Ch. Stoyanov, Phys. Lett. B **586**, 213 (2004).

[27] N. Tsoneva, H. Lenske, and Ch. Stoyanov, Nucl. Phys. A **731**, 273 (2004).

[28] N. Tsoneva and H. Lenske, Phys. Rev. C **77**, 024321 (2008).

[29] K. Yoshida, Phys. Rev. C **82**, 034324 (2010).

[30] J. P. Ebran, E. Khan, T. Nikšić, and D. Vretenar, Nature (London) **487**, 341 (2012).

[31] J. P. Ebran, E. Khan, T. Nikšić, and D. Vretenar, Phys. Rev. C **90**, 054329 (2014).

[32] J.-P. Ebran, E. Khan, R. D. Lasseri, and D. Vretenar, Phys. Rev. C **97**, 061301(R) (2018).

[33] J.-P. Ebran, M. Girod, E. Khan, R. D. Lasseri, and P. Schuck, Phys. Rev. C **102**, 014305 (2020).

[34] P. Marević, J.-P. Ebran, E. Khan, T. Nikšić, and D. Vretenar, Phys. Rev. C **97**, 024334 (2018).

[35] P. Marević, J.-P. Ebran, E. Khan, T. Nikšić, and D. Vretenar, Phys. Rev. C **99**, 034317 (2019).

[36] H. Liang, T. Nakatsukasa, Z. Niu, and J. Meng, Phys. Rev. C **87**, 054310 (2013).

[37] T. Nikšić, N. Kralj, T. Tutis, D. Vretenar, and P. Ring, Phys. Rev. C **88**, 044327 (2013).

[38] A. Bjelčić and T. Nikšić, Comput. Phys. Commun. **253**, 107184 (2020).

[39] T. Nakatsukasa, T. Inakura, and K. Yabana, Phys. Rev. C **76**, 024318 (2007).

[40] P. Avogadro and T. Nakatsukasa, Phys. Rev. C **84**, 014314 (2011).

[41] M. Stoitsov, M. Kortelainen, T. Nakatsukasa, C. Losa, and W. Nazarewicz, Phys. Rev. C **84**, 041305(R) (2011).

[42] T. Nikšić, D. Vretenar, and P. Ring, Phys. Rev. C **78**, 034318 (2008).

[43] T. Duguet, Phys. Rev. C **69**, 054317 (2004).

[44] Y. Tian, Z. Y. Ma, and P. Ring, Phys. Lett. B **676**, 44 (2009).

[45] J. F. Berger, M. Girod, and D. Gogny, Comput. Phys. Commun. **63**, 365 (1991).

[46] I. Hamamoto, H. Sagawa, and X. Z. Zhang, Phys. Rev. C **56**, 3121 (1997).
[47] M. Vandebrouck, J. Gibelin, E. Khan, N. L. Achouri, H. Baba, D. Beaumel, Y. Blumenfeld, M. Caamano, L. Caceres, G. Colo, F. Delaunay, B. Fernandez-Dominguez, U. Garg, G. F. Grinyer, M. N. Harakeh, N. Kalantar-Nayestanaki, N. Keeley, W. Mittig, J. Pancin, R. Raabe *et al.*, Phys. Rev. Lett. **113**, 032504 (2014).
[48] E. Becheva, Y. Blumenfeld, E. Khan, D. Beaumel, J. M. Daugas, F. Delaunay, Ch-E. Demonchy, A. Drouart, M. Fallot, A. Gillibert, L. Giot, M. Grasso, N. Keeley, K. W. Kemper, D. T. Khoa, V. Lapoux, V. Lima, A. Musumarra, L. Nalpas, E. C. Pollacco *et al.*, Phys. Rev. Lett. **96**, 012501 (2006).
[49] M. Buenerd, D. Lebrun, Ph. Martin, P. de Saintignon, and C. Perrin, Phys. Rev. Lett. **45**, 1667 (1980).
[50] U. Garg, P. Bogucki, J. D. Bronson, Y.-W. Lui, and D. H. Youngblood, Phys. Rev. C **29**, 93 (1984).
[51] D. Pena Arteaga, E. Khan, and P. Ring, Phys. Rev. C **79**, 034311 (2009).
[52] J. Kvasil *et al.*, J. Phys.: Conf. Ser. **580**, 012053 (2015).
[53] D. R. Bes and R. A. Broglia, Nucl. Phys. **80**, 289 (1966).
[54] R. A. Broglia and D. R. Bes, Phys. Lett. B **69**, 129 (1977).
[55] A. Vitturi, L. Ferreira, P. D. Kunz, H. M. Sofia, P. F. Bortignon, and R. A. Broglia, Nucl. Phys. A **340**, 183 (1980).
[56] E. Khan, N. Sandulescu, N. V. Giai, and M. Grasso, Phys. Rev. C **69**, 014314 (2004).
[57] M. Matsuo, K. Mizuyama, and Y. Serizawa, Europhys. J. A **25**, 563 (2005).
[58] H. Shimoyama and M. Matsuo, Phys. Rev. C **84**, 044317 (2011).
[59] K. Yoshida *et al.*, Phys. Scr. **T125**, 45 (2006).
[60] T. Duguet, B. Bally, and A. Tichai, Phys. Rev. C **102**, 054320 (2020).